

Magnesium isotope evidence for enhanced crustal reworking in lowermost Cambrian sedimentary rocks (Kazakhstan)

Jessica A. Stammeier^{a,b,*}, Dorothee Hippler^a, Oliver Nebel^c, Martin Dietzel^a

^a Institute of Applied Geosciences, Graz University of Technology, Rechbauerstraße 12, 8010, Graz, Austria

^b GFZ German Research Centre for Geosciences, Telegrafenberg, 14473, Potsdam, Germany

^c School of Earth, Atmosphere and Environment, Monash University, Clayton, VIC, 3800, Australia

ABSTRACT

The transition from the Proterozoic to the Phanerozoic Eon was accompanied by the rise of metazoan life, a key and unique biogeochemical milestone in Earth's history. Concomitant continental re-organization and collision were associated with enhanced continental reworking and changes in global ocean currents, with profound impacts on continental weathering rates, riverine run-off and associated changes in the ocean nutrient budget. The causal relationship between the geological re-organisation of continents and the biologic evolution of marine life, however, remains elusive. In this study, we investigate phosphatic shallow-water sedimentary successions from Kazakhstan, which host key marker horizons from the Precambrian-Cambrian (Pc-C) boundary. We show that a rapid change (over ca. 3 Myrs) towards heavier stable Mg isotope compositions of the phosphatic sedimentary deposits in Kazakhstan, which we consider representative for contemporaneous ocean chemistry, co-varies with changes in radiogenic Sr isotope signatures. We propose that ocean chemistry at the Pc-C boundary, represented through this co-variation, was strongly affected by continental re-organization and associated weathering, which, in analogy, would have affected ocean nutrient levels. A rapid reversal of isotope compositions towards signatures similar to those prior to the isotope excursion likely reflects the fading influence of weathering and a buffering of water-rock interactions during oceanic spreading. We conclude that, based on the positive, coupled $^{87}\text{Sr}/^{86}\text{Sr}$ - $\delta^{26}\text{Mg}$ isotope spike in ocean water chemistry, a link between Gondwana re-organization at the Pc-C boundary and the marked change in marine fauna seems plausible.

1. Introduction

The Precambrian-Cambrian (Pc-C) transition has long been recognized as a critical point in Earth's history, marking the rise of metazoan life following the first aquatic mass extinction of the Ediacaran fauna at ca. 541 Ma (e.g., Darroch et al., 2018; Laflamme et al., 2013). Most prominent environmental and geological factors associated with this change in the biosphere are (I) oceanic and atmospheric oxygenation; (II) crustal reworking (continental weathering, erosion) and high nutrient supply into the marine realm with subsequent chert and phosphate deposition; (III) perturbation to nutrient cycling; and (IV) the re-assembly of continental masses (e.g., Zhang et al., 2014; Smith and Harper, 2013, and references therein). Despite decades of research, causal relationships between the biologic, ecologic and geologic features and respective timing of oxygenation relative to the Pc-C transition remain controversial, and an individual trigger initiating the secular change from Ediacaran to Cambrian fauna is yet to be identified (Fox, 2016).

Increasing $^{87}\text{Sr}/^{86}\text{Sr}$ in seawater during the late Neoproterozoic has been linked to the exposure of radiogenic, cratonic crust during the break-up of Rodinia (Halverson et al., 2009) and enhanced weathering rates and continental run-off (Derry et al., 1994). A sharp, positive

excursion in Sr isotopes at the Pc-C transition has been suggested to reflect a higher influx of evolved, crustal material (Burns et al., 1994), which was subsequently counterbalanced by increased hydrothermal activity. More recent studies, which also recognized a positive excursion (e.g., Li et al., 2013), however, dismissed very radiogenic Sr isotopes as poor preservation and/or diagenetic alteration, and with this their environmental significance. Yet, this extremely positive excursion in radiogenic Sr isotopes can be observed at different locations worldwide (Brasier et al., 1996; Derry et al., 1994; Halverson et al., 2010; Nicholas, 1996; Sawaki et al., 2008). A contemporaneous positive $^{87}\text{Sr}/^{86}\text{Sr}$ peak has recently been recorded in early Cambrian carbonate and phosphorite sections of the Malyi Karatau, Kazakhstan (Stammeier et al., 2019a), rendering these sections a suitable archive for further investigations regarding the potential causes of the excursion. The sedimentary rocks were deposited during the Pc-C episode in a former shallow-water basin. They likely represent global ocean evolution and have been interpreted to reflect enhanced crustal reworking, i.e., continental weathering and erosion (Stammeier et al., 2019a). This temporal relationship supports a scenario in which changes in biodiversity were linked to geodynamic responses of plate re-organization. Whilst detailed relations are far more complex, this would generally link the evolution of Cambrian biota to passive margin dynamics.

* Corresponding author. Institute of Applied Geosciences, Graz University of Technology, Rechbauerstraße 12, 8010, Graz, Austria.

E-mail address: jessica.stammeier@gfz-potsdam.de (J.A. Stammeier).

A test for the degree and impact of continental weathering to ocean chemistry is potentially captured in distinct stable isotope signatures of authigenic, abiotic shallow-water sedimentary rocks. Magnesium is a major component during chemical weathering and abiotic carbonate precipitation (Berner et al., 1983). Thus, the Mg isotope composition of seawater is largely influenced by flux imbalances between weathering and carbonate precipitation processes; detailed knowledge of these influences has been used to trace changes in the weathering regime before (e.g., Kasemann et al., 2014; Pogge von Strandmann et al., 2014; Pokrovsky et al., 2011; Tipper et al., 2006a, 2006b; Wimpenny et al., 2014).

Herein, we present new Mg isotope data for the Kazakhstan section and compare them with previously reported radiogenic Sr isotope variations (Stammeier et al., 2019a). Combined with published global $^{87}\text{Sr}/^{86}\text{Sr}$ seawater signatures, we evaluate the consequences of differences in Mg and Sr isotopes in a dynamic time-dependent state model and aim to validate these results with plausible causes for seawater excursions in light of enhanced weathering rates, carbonate precipitation and hydrothermal activity.

2. Sample description

The Koksau section and the herein investigated samples have previously been described in detail by Stammeier et al. (2019a) in terms of petrography and geochemistry. A summary of the investigated sample material and micrographs can be found in Appendix A. Briefly, the section (43° 39' 13.0" N, 69° 38' 11.0" E) is located in the Malyi Karatau mountain range, South Kazakhstan and comprises sedimentary rocks of the Fortunian and Stage 2 of the lower Cambrian (541 - 521 Ma, Figs. 1 and 2). The 50-m-long profile crops out along an abandoned exploration trench comprising a consecutive sequence of the Chulakta Formation (Fm.), which consists in its lower part mainly of cherts and phosphorites. The investigated samples belong to the two lowermost members of the Chulakta Fm., (1) the Aksai Chert, bedded, dark-colored cherts with variable dolomitic and phosphatic content, and (2) the Lower Phosphorite, cross-bedded, granular phosphorites with a calcite and/or dolomite matrix. Internal structure, element and isotope systematics classified these rocks as near primary sedimentary rocks (see detailed discussion in Stammeier et al., 2019a; Fig. A1).

3. Methodology

To evaluate the effect of our leaching procedure a two-step acid leaching approach, using 0.05 mol l^{-1} and 3 mol l^{-1} HNO_3 ,

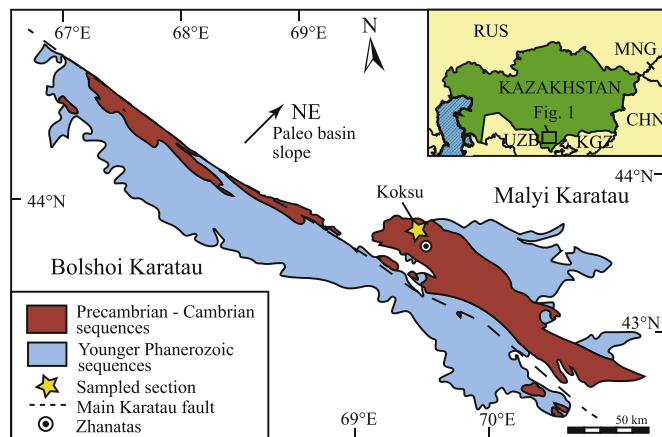


Fig. 1. Schematic geologic map of the Malyi and Bolshoi Karatau Mountain range (simplified after Eganov and Sovetov, 1986). The Koksau section (43.653611, 69.636389, WGS84) is located at the margin of a former shallow-water basin.

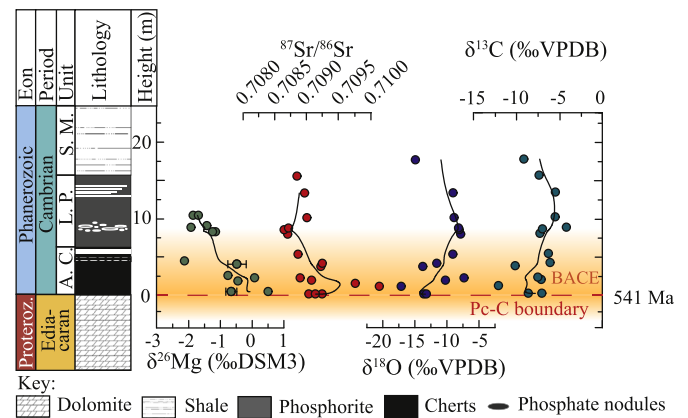


Fig. 2. Compiled isotope profile of the investigated Koksau section. Both Mg-Sr and C-O isotopes display the same temporal trend, calculated as the moving average (black line). The orange shading indicates the timing of the basal Cambrian carbon event (BACE). Strontium, C and O isotope data are taken from Stammeier et al. (2019a). Ky. Fm = Kyrshabakty formation, AC = Aksai Chert, LP = Lower Phosphorite, SM = Shale Member after (Heubeck et al., 2013). If not indicated otherwise, uncertainty (2 SD) is within symbol size. (For interpretation of the references to color in this figure legend, the reader is referred to the Web version of this article.)

respectively, was employed in a pre-study. These leaching experiments were conducted on two selected samples with different matrix (dolomite vs. calcite) and texture (phos-grainstone (KO 10) vs. phos-rudstone (KO 13)). From each sample, ca. 20 mg powder was microdrilled. The powders were leached in 0.05 mol l^{-1} HNO_3 , rinsed with Milli-Q® three times, and dried down. Each dried sample was then leached in 3 mol l^{-1} HNO_3 and subsequently rinsed with Milli-Q® three times. Each leachate, incl. the Milli-Q®-rinse, was decanted, evaporated and then digested in 2 mol l^{-1} HNO_3 for Mg separation. The results are depicted in Fig. 3 and reveal identical Mg isotope composition for both acid leachates within a reproducibility of $\pm 0.10\text{‰}$ for $\delta^{26}\text{Mg}$, expressed as 2 S.D. Based on these results, bulk sample powders were leached in 3 mol l^{-1} HNO_3 for 24 h at 70°C , capturing both carbonate fluorapatite (CFA) and carbonate phases (calcite and dolomite). This acid-soluble fraction was used for all consecutive elemental analysis and separations. The Mg fraction was purified with a two-step ion exchange chemistry using BioRad AG50-X12 resin and HNO_3 and HCl as eluent agents (after Pogge von Strandmann, 2008; Wombacher et al., 2009). For method and analytical details please compare (Stammeier et al., 2019b). In brief, Ca was eliminated by passing the samples over the columns using 15 ml of 2 mol l^{-1} HNO_3 . All other interfering cations were eluted using 30 ml of 0.4 mol l^{-1} HCl . Magnesium was then collected in 5 ml 5 mol l^{-1} HCl . Yields and interferences were routinely

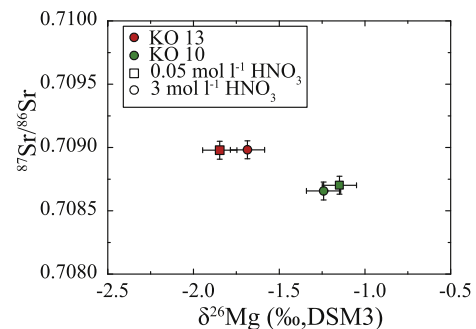


Fig. 3. Mg and Sr isotope composition of two samples treated with weak acid (0.05 mol l^{-1} HNO_3 ; squares) and stronger acid (3 mol l^{-1} HNO_3 ; circles). Error bars for $\delta^{26}\text{Mg}$ are $\pm 0.10\text{‰}$ and refer to the reproducibility of reference material Cambridge-1 (Romil Ltd., Cambridge, UK). Sr isotope values and respective uncertainties from (Stammeier et al., 2019a).

tested to ensure a complete recovery of Mg. Measurements were performed on a Nu Plasma II MC-ICP-MS (Nu Instruments, Wrexham, UK) at the NAWI Graz, Central Lab for Water, Minerals and Rocks (NAWI Graz Geocenter, Austria). Analyses were typically performed in wet plasma with a sensitivity of ca. 12.5 V for 500 $\mu\text{g ml}^{-1}$ on ^{24}Mg using a 0.1 ml/min nebulizer. Data acquisition consisted of 1 block with 25 cycles with an integration time of 5 s each. The background was determined by 10 s integration time at half masses, i.e., with 0.5 amu offset before each block (cf. Aciego et al., 2009; Jackson and Attalla, 2010). Measurements were performed with standard-sample-bracketing (SSB) and are reported in the δ -notation as per mil (‰) deviation relative to DSM3 standard. Concentrations of reference materials and samples were adjusted to match within 10%. Repeated measurements of reference material Cambridge-1 (Cam-1, Romil Ltd., Cambridge, UK) yielded $-2.64 \pm 0.10\text{‰}$ for $\delta^{26}\text{Mg}$ and $-1.36 \pm 0.04\text{‰}$ for $\delta^{25}\text{Mg}$ (2 SD, $n = 23$), identical to previously reported values by Mavromatis et al. (2014). Reproducibility of the total procedure was tested using JDo-1, which yielded $-2.47 \pm 0.10\text{‰}$ for $\delta^{26}\text{Mg}$ and $-1.30 \pm 0.02\text{‰}$ for $\delta^{25}\text{Mg}$ (2 SD, $n = 3$). Procedural blank was typically below 50 ng l^{-1} for Mg and thus negligible.

4. Results

4.1. Stable Mg isotope record throughout the sedimentary profile

Magnesium isotope analyses of the acid-soluble fraction yield $\delta^{26}\text{Mg}$ values ranging from -2.3‰ to 0.5‰ (relative to the DSM3 reference material) with a mean of $-1.0 \pm 0.2\text{‰}$ (2 SE, $n = 13$). The observed temporal trend of decreasing $\delta^{26}\text{Mg}$ towards younger samples appears to correlate considerably with previously investigated $^{87}\text{Sr}/^{86}\text{Sr}$ values (Fig. 2, Appendix A; Table A1; Stammeier et al., 2019a). However, a plot of $\delta^{26}\text{Mg}$ vs. $^{87}\text{Sr}/^{86}\text{Sr}$ displays no correlation, with an $R^2 < 0.1$ (Fig. 4, inset A), indicating that these isotopes may not reflect the same genetic process. Yet, the evident temporal evolution in both proxies indicates a common overall trigger in isotope variability that possibly affects both elements differently. Moreover, $\delta^{26}\text{Mg}$ values are anti-correlated with $\delta^{13}\text{C}_{\text{carb}}$ and $\delta^{18}\text{O}_{\text{carb}}$ (Fig. 2), the latter reflecting ambient environmental and depositional conditions. To the authors' knowledge, these $\delta^{26}\text{Mg}$ are the highest reported values in dolomites to date. Geske et al. (2015) investigated suites of dolomites from different environmental settings and reported a considerably large range of $\delta^{26}\text{Mg}$ values ranging from -2.49‰ to -0.45‰ , where the highest values were found in non-marine and hydrothermal settings. Positive $\delta^{26}\text{Mg}$ values, as found in two samples from the present study, are typically a feature only exhibited by silicates (Farkas et al., 2013; Higgins and Schrag, 2010). In general, $\delta^{26}\text{Mg}$ in dolomite mainly reflects the composition of the source fluid and is only insignificantly altered during diagenetic alteration or low grade metamorphism (Geske et al.,

2015b, 2015a). Accordingly, the sediments studied here have most likely been deposited in a shallow-marine environment (Stammeier et al., 2019a), and likely reflect changing $\delta^{26}\text{Mg}$ source composition. As a result, the correlation between $\delta^{26}\text{Mg}$ and $\delta^{18}\text{O}$ values of these sediments from Kazakhstan is insignificant with an $R^2 < 0.1$ (Fig. 4, inset B).

4.2. $\delta^{26}\text{Mg}$ and $^{87}\text{Sr}/^{86}\text{Sr}$ ocean budgets in a time-dependent dynamic state model

The significance and meaning of both, stable Mg and radiogenic Sr isotopes can be tested with a mass balance model that equates elemental and isotopic input and output fluxes for the past ocean basin (Tipper et al., 2006b). To reconstruct the radiogenic Sr and Mg isotope evolution during the Pc-C transition, we used a time-dependent dynamic state model based on the equation

$$\frac{dNR_{\text{sw}}}{dt} = \sum F_{\text{in}} R_{\text{in}} - \sum F_{\text{out}} R_{\text{out}} \quad (1)$$

describing the isotopic evolution R_{sw} , where SW denotes seawater, of reservoir N as a function of the fluxes F in and out of the reservoir with the attributed isotope composition R (e.g., Richter et al., 1992).

Considering the residence time (τ) in Myr as

$$\tau = N_{(t)}/\Sigma F_{\text{in}} \quad (2)$$

the time-dependent evolution can be described by

$$R_{\text{sw}}(t) = R_{\text{sw-SSX}} - (R_{\text{sw-SSX}} - R_{\text{sw-t0}})e^{-(\Delta t)/\tau} \quad (3)$$

(detailed mathematical derivation is given by Hodell et al., 1989), where X denotes the respective steady state conditions for Mg or Sr (see below). Note that $N_{(t)}$ includes changes of the reservoir size in response to changing fluxes.

As a first order approximation, the main source to the Mg budget in seawater is riverine influx (F_R), which is counterbalanced by output via carbonate precipitation from seawater (F_C) and hydrothermal removal through interaction of sea water with mid ocean ridge basalts (MORB; F_H). Here, we can assume that $R_{\text{sw}} = R_H$ as Mg isotope fractionation through hydrothermal removal is generally negligible (de Villiers et al., 2005; Pogge von Strandmann et al., 2014). This yields the equation for steady state conditions ($R_{\text{sw-ss}}$) for Mg in seawater:

$$R_{\text{sw-ssMg}} = \frac{F_R R_R - F_C R_C}{F_R - F_C} \quad (4)$$

For the Sr isotope ocean budget, carbonate precipitation constitutes the main sink of Sr (Palmer and Edmond, 1989). Radiogenic Sr isotopes do not fractionate during carbonate precipitation, thus we can set $R_{\text{sw}} = R_{\text{out}}$. The remaining fluxes into the ocean are mainly of riverine (F_R), hydrothermal (F_H) and diagenetic (F_D) origin. Assuming $dR_{\text{sw}}/dt = 0$, Equation (1) yields the steady state equation ($R_{\text{sw-ssr}}$) for Sr in

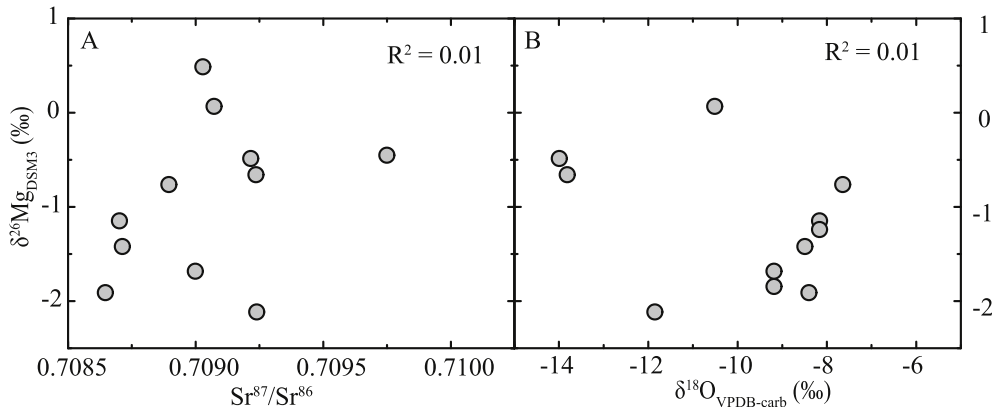


Fig. 4. Cross plots of $\delta^{26}\text{Mg}$ vs. $^{87}\text{Sr}/^{86}\text{Sr}$ and $\delta^{18}\text{O}$. Note that the bulk of data does not show any correlation.

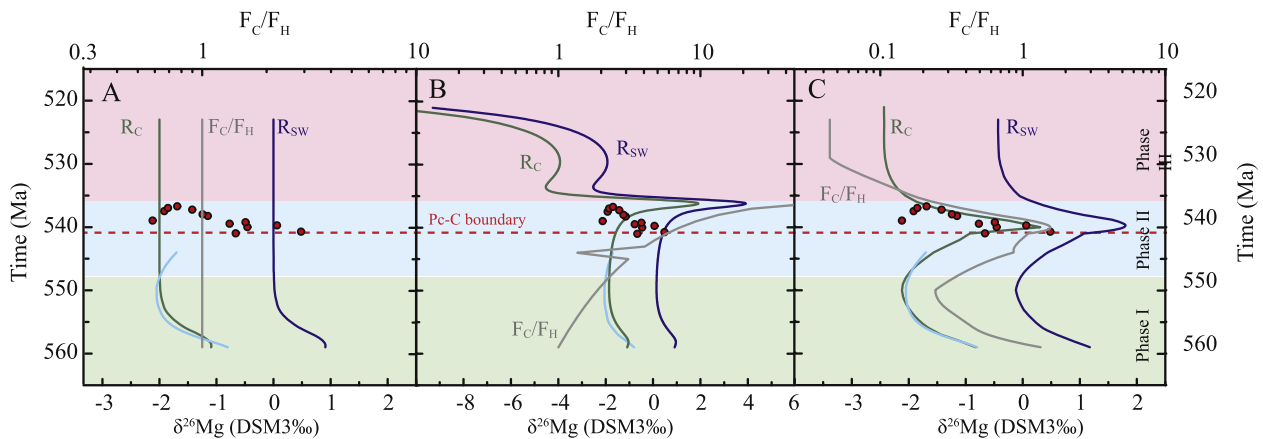


Fig. 5. Calculated Mg isotope values in a time-dependent dynamic state model. Red circles indicate isotope ratios measured in early Cambrian Kazakh strata (this study). Bright blue line: $\delta^{26}\text{Mg}$ values of dolomites from the Siberian platform taken from Pokrovsky et al. (2011). Note that the age of these values could only be estimated linearly. Blue line (R_{SW}) represents modelled $\delta^{26}\text{Mg}$ seawater evolution, with the respective carbonates (R_{C} , green line), in response to dynamic carbonate removal (F_{C}) and hydrothermal activity (F_{H}), shown as $F_{\text{C}}/F_{\text{H}}$ (grey line). Note the different scales of the primary and secondary abscissae in the insets. Inset A: modelled $\delta^{26}\text{Mg}$ at steady state conditions. Inset B: Modelled $\delta^{26}\text{Mg}$ show significant variation when carbonate removal F_{C} is increased. The reversed trend of R_{SW} at 536 Ma is produced when $F_{\text{C}} > F_{\text{R}}$. Inset C: ‘best-fit’ of modelled $\delta^{26}\text{Mg}$. Note that R_{R} remains constant up to 545 Ma. (For interpretation of the references to color in this figure legend, the reader is referred to the Web version of this article.)

seawater:

$$R_{\text{SW-SSr}} = \frac{F_{\text{R}}R_{\text{R}} + F_{\text{H}}R_{\text{H}} + F_{\text{D}}R_{\text{D}}}{F_{\text{R}} + F_{\text{H}} + F_{\text{D}}} \quad (5)$$

The model calculates the Mg and Sr isotope composition of the ocean in iterative steps of 1 Myr covering the time from mid-Ediacaran (560 Ma) to the Early Cambrian (521 Ma). This was done in two general approaches: (i) using the steady state conditions to evaluate the responses of the reservoir to steady changes; and (ii) applying a dynamic change of parameters, in order to achieve a ‘best fit’ of the observed data (Figs. 5 and 6).

4.2.1. $\delta^{26}\text{Mg}$ in seawater and carbonates

Experimental studies have shown that dolomite formation (assuming ideal stoichiometry) constitutes the majority of the Mg sink through carbonate removal, and can be estimated to account for $\Delta^{26}\text{Mg}_{\text{Dol-SW}}$ of ca. -1.7 to -2.7 ‰ (Geske et al., 2015b; Higgins and Schrag, 2010; Li et al., 2015). Hence Mg isotopes in carbonates can only indirectly reflect seawater composition. Thus, $\delta^{26}\text{Mg}$ of carbonates was calculated for each iterative step as a function of changing seawater composition. The $\Delta^{26}\text{Mg}_{\text{Dol-SW}}$ was kept constant throughout the model using an average value of $\Delta^{26}\text{Mg}_{\text{Dol-SW}} = 2.0$ ‰. For simplification we consider this isotope fractionation factor to be a representative estimate for global carbonate removal, given the diversity of settings and parameters, e.g., temperature. The isotope fractionation factor between Mg

calcite (limestone) and precipitation solution would be larger with $\Delta^{26}\text{Mg}_{\text{CC-SW}}$ of ca. -3.6 ‰ (Fantle and Higgins, 2014). However, given stoichiometry, this has a smaller impact on Mg mass balance. Assuming a greater proportion of Mg-calcite on overall carbonate removal, the removal of light isotopes during times of increased carbonate precipitation would be enhanced, producing a Mg_{SW} evolution with higher amplitudes (Fig. 7). $\delta^{26}\text{Mg}$ of the riverine influx was set to $R_{\text{R}} = -0.5$ ‰, representing silicate dominated weathering and kept constant (see Section 5.1; Tipper et al., 2006; Wimpenny et al., 2014). Tipper et al. (2006) suggest that during times of increased dolomitization, $\delta^{26}\text{Mg}_{\text{SW}}$ could have been up to 1.5 ‰ heavier than present-day seawater. Accordingly, initial $\delta^{26}\text{Mg}_{\text{SW}}$ was set to $+0.8$ ‰.

For this seawater $\delta^{26}\text{Mg}$ model, the riverine influx F_{R} and removal through carbonate precipitation F_{C} were changed as a function of time, as continental weathering and carbonate deposition were likely the strongest influences on $\delta^{26}\text{Mg}_{\text{SW}}$ at that time. With the condition that $\Sigma F_{\text{in}} = \Sigma F_{\text{out}}$, F_{H} is defined by the difference of $F_{\text{R}} - F_{\text{C}}$. The initial values are reported in Table 1. The initial magnitude of riverine Mg input (F_{R}) is adapted from Wilkinson and Algeo (1989) and removed from the ocean by F_{H} and F_{C} in equal proportions.

For Mg, leaving all fluxes and isotope ratios unchanged, R_{SW} initially decreases and reaches steady state conditions after ca 10 Myr at 549 Ma, converging a $R_{\text{SW}} = 0$ ‰ and thus R_{C} of -2.0 ‰ (Fig. 5, inset A). Although, these initial 10 Myr broadly match the magnitude of the observed data from Pokrovsky et al. (2011), the observed Mg values in

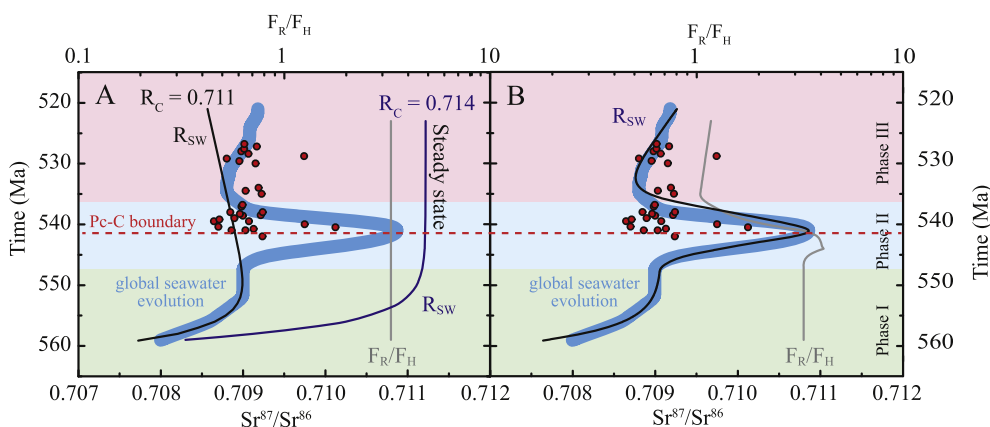


Fig. 6. Calculated Sr isotope values in a time-dependent dynamic state model. Red circles indicate isotope ratios measured in early Cambrian Kazakh strata. Thick blue line indicates recorded $^{87}\text{Sr}/^{86}\text{Sr}$ seawater evolution as compiled by Stammeier et al. (2019a) and references therein. Inset A: modelled $^{87}\text{Sr}/^{86}\text{Sr}$ seawater at steady state conditions, calculated using $R_{\text{R}} = 0.714$ (blue line) and $R_{\text{R}} = 0.711$ (black line). Inset B: modelled $^{87}\text{Sr}/^{86}\text{Sr}$ seawater evolution matches the observed $^{87}\text{Sr}/^{86}\text{Sr}$ seawater evolution. (For interpretation of the references to color in this figure legend, the reader is referred to the Web version of this article.)

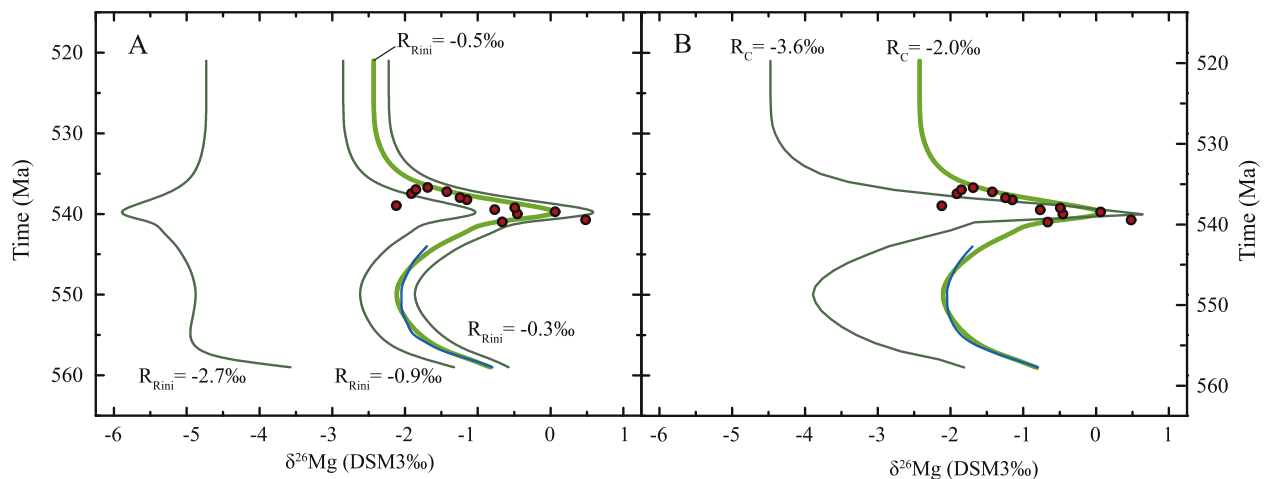


Fig. 7. Modelled $\delta^{26}\text{Mg}$ in carbonates (R_C) using different parameters. Inset A: evolution of R_C when applying different riverine (R_R) input values, representing carbonate, silicate, generally or mixed weathering dominated endmembers, in comparison to 'best-fit' results (thick green line). Inset B: considering a larger fractionation factor, e.g., representing calcite precipitation, the amplitude of the modelled $\delta^{26}\text{Mg}$ becomes significantly larger. Note that for this latter calculation same parameters as for the 'best-fit' were used. (For interpretation of the references to color in this figure legend, the reader is referred to the Web version of this article.)

Table 1
Parameter values used in the time-dependent dynamic state model.

	Parameter	Sr ¹	Mg ⁴
Source*:	F_R (mol yr ⁻¹)	$3.3 \cdot 10^{10}$	$5.6 \cdot 10^{12}$
	F_D (mol yr ⁻¹)	$0.3 \cdot 10^{10}$	$2.8 \cdot 10^{12}$
	F_H (mol yr ⁻¹)	$1.0 \cdot 10^{10}$	$2.8 \cdot 10^{12}$
	N (mol)	$1.25 \cdot 10^{17}$	$7.3 \cdot 10^{19}$
		$^{87}\text{Sr}/^{86}\text{Sr}$ ^{2,3}	$\delta^{26}\text{Mg}$ ^{5,6,7}
Isotope ratios*:	R_R	0.711	-0.5‰
	R_C	0.708	-2.0‰
	R_H	0.703	
	R_N		0.8‰

* Subscript refers to the respective reservoir with R = riverine, D = diagenetic, H = hydrothermal, C = carbonate.

¹ Richter et al. (1992).

² Halverson et al. (2010).

³ Wilson (1989).

⁴ Wilkinson and Algeo (1989).

⁵ Wimpenny et al. (2014).

⁶ Tipper et al., 2006.

⁷ Pokrovsky et al. (2011).

this study suggest much heavier R_{SW} thereafter. Shifting R_{SW} towards lighter values is most easily achieved by decreasing carbonate removal F_C (Fig. 5, inset B). Given the assumed high R_R (-0.5‰), the diluting effect of riverine input on R_{SW} ($R_{SW} = 0.1‰$ at 547 Ma) is negligible at that time. However, around 547 Ma this trend was reversed, causing the observed increase in R_C and extremely high values at the Pc-C boundary.

Our model shows, that the Mg ocean budget requires a very dynamic change of parameters, including an incongruent increase of F_R and F_C . Taking all of these findings together, a 'best-fit' of parameters was modelled (Fig. 5, inset C). This 'best-fit' model can be divided in three phases (Fig. 5, inset C). In Phase I, 560 - 547 Ma, as described above, Mg removal through carbonate formation (F_C) steadily decreases while weathering rates are generally elevated. This causes the steady decrease in $\delta^{26}\text{Mg}_{SW}$. In Phase II, 546-536 Ma, this decrease was reversed by steadily climbing F_C , causing an increase in $\delta^{26}\text{Mg}_{SW}$. Around 544 Ma this process was balanced by increasing weathering rates, F_R , accounting for a doubling of F_R within ca. 3 Myr. Thereafter, F_C and F_R rates decrease again, coupled with increasing hydrothermal removal F_H . For Phase III, 536-520 Ma, evidence of true data is missing. Thus, parameters from 536 Ma, the last observed data point from this study,

were kept stable converging steady state conditions. Overall, the three phases mark an increase in $\delta^{26}\text{Mg}_{SW}$ with increase over ca. 15 Myr and a subsequent decrease over 5 Myr with a final balance over the remaining 22 Myr, all mainly controlled by long-term changes of carbonate precipitation rates and swift increases of weathering rates.

4.2.2. $^{87}\text{Sr}/^{86}\text{Sr}$ seawater evolution

Using the steady state condition for Sr in seawater (i.e., Equation (5)) in Equation (3) we forced the riverine (F_R) and hydrothermal (F_H) fluxes and left the diagenetic flux (F_D) constant. The initial fluxes F_{in} are reported in Table 1 and represent present day values. Isotope ratios R_{in} were chosen as $R_R = 0.711$ to represent increased continental weathering rates, $R_D = 0.708$ and $R_H = 0.703$ according to $^{87}\text{Sr}/^{86}\text{Sr}$ seawater and mantle evolution during the Ediacaran, respectively (Halverson et al., 2010; Wilson, 1989). Leaving all parameters unchanged, R_{SW} rapidly increases, converging $R_{SW} = 0.7091$ and reaching near-steady state after ca. 20 Myr (Fig. 6, inset A). Similar to Mg, steady state conditions match the initial phase of the observed Sr seawater evolution well, up to 547 Ma. Applying the same parameter changes as for the Mg ocean budget, i.e., changing F_C and a swift increase in F_R , however does not satisfy the observed dynamics of the Sr seawater evolution. Other than for Mg, F_R is the most powerful parameter driving R_{SW} towards higher Sr isotope values, counterbalanced mainly by F_H , causing a reversed trend towards lower Sr isotope values. However, a steady increase in F_R does not recreate the first slow increase followed by a rapid positive excursion as observed in the Sr seawater evolution (Phase II). This could be achieved by a change in weathered rock-type, i.e., from a dominance of less radiogenic rock types ($R_R = 0.711$) towards more radiogenic rock types ($R_R = 0.714$). This could either be due to a decreased proportion of chemical weathering of carbonates, or pronounced weathering of granitic material. As shown above by the Mg box model (see Section 4.2.1), chemical weathering of carbonates could not have been a contributing factor to riverine run-off, arguing for an increased amount of basalt weathering during Phase I, which would also exhibit a non-radiogenic isotope signature. Alternatively, if R_R was 0.714 from the beginning, F_H would need to be significantly higher to balance the riverine input, causing the observed slower increase (Fig. 6, inset A, blue line). However, we dismissed the latter possibility, as this would require very sudden shifts in hydrothermal activity.

Thus, in the 'best-fit' model the isotope ratio of the riverine input was adjusted, assuming less radiogenic weathered material in the initial weathering phase followed by an increasing proportion of radiogenic

material as continental denudation progresses, favoring increased ‘mineral reactivity’ (cf. [Caves Rugenstein et al., 2019](#)). This ‘best-fit’ model also resembles the three temporal phases employed for the Mg isotope systematics (Fig. 6, inset B). In Phase I, 560–547 Ma, all parameters remain in steady state at generally high weathering rates, causing the R_{SW} to slowly increase. In Phase II, 546–536 Ma, as continental erosion progresses, more radiogenic rocks are exposed. Together with rapidly increasing F_R , this causes the spike in R_{SW} . The rapid increase in F_R stops at 547 Ma and returned to initial values, further balanced by the continuously increasing F_H in Phase II. In Phase III, 535–521 Ma, similar to the Mg ocean budget, F_C and F_H remain stable, with only F_R slightly increasing. In this dynamic ‘best-fit’, the model successfully recreates the observed Sr seawater evolution, matching both magnitude and short duration of the observed peak.

5. Discussion

5.1. The significance of $\delta^{26}\text{Mg}$ composition of the riverine input

Isotopically heavy $\delta^{26}\text{Mg}$ seawater values can be caused by either preferential removal of light Mg isotopes, i.e. during extreme dolomitization events, or input of heavy isotopes, i.e. through silicate dominated riverine influx. However, our box model needs to be confirmed by both, Sr and Mg fluxes. Thus, although dolomitization may contribute to the scatter in Mg–Sr isotope co-variations, it cannot be the main reason for the coupled isotope excursion, as this wouldn’t cause such extreme changes in the Sr isotope evolution. Despite uncertainty in the input parameters, it is apparent that the isotope modelling recreates the observed amplitude at the Pc-C transition.

[Tipper et al. \(2006\)](#) showed that modern rivers draining silicate rocks can be as heavy as -0.3‰ in Mg isotopes and rivers draining carbonate rocks record values as low as -2.7‰ . In weathering dominated rivers, such as the Ganges-Brahmaputra and/or Indus that drain mixed lithologies of the Himalaya, these two endmembers add to a combined riverine $\delta^{26}\text{Mg}$ of -0.9‰ . To evaluate the significance of the isotope ratio of riverine influx (R_C), we increase carbonate removal (F_C) up to 90% of the total influx and combined this with three different possible isotope ratios (R_R) of the riverine influx to represent the different endmembers from (a) carbonate dominated weathering with a $\delta^{26}\text{Mg}$ value of -2.7‰ , (b) silicate dominated weathering with a $\delta^{26}\text{Mg}$ value of -0.3‰ , and (c) a $\delta^{26}\text{Mg}$ value of -0.9‰ representing a lithologically mixed weathering dominated river (Fig. 7, inset A; [Tipper et al., 2008](#)). For (a) calculated carbonate $\delta^{26}\text{Mg}$ values are unrealistically low with an average of $-4.9 \pm 0.7\text{‰}$ (2SD, $n = 39$) and display the opposite trend of the observed Mg evolution. Thus, we argue that weathering of carbonates could not have played a significant role during the Pc-C time period. In turn, as suggested in the ‘best-fit’ model for Sr seawater evolution, a shift from the weathering of basalt dominated catchment towards a granite dominated one would not affect the $\delta^{26}\text{Mg}$ composition of riverine run-off. Using the $\delta^{26}\text{Mg}$ value of the silicate weathering dominated Scenarios (b) and (c), it was possible to recreate a more sensible trend (Fig. 7). The ‘best-fit’ was calculated with an R_R value of -0.5‰ for $\delta^{26}\text{Mg}$, representing an intermediate value between a purely silicate dominated weathering (Scenario b) regime and a lithologically mixed weathering dominated regime (Scenario c), which would validate the observed Sr–Mg isotope systematics.

5.2. Mg isotopes as a palaeo-environmental proxy in ancient sediments

Although Mg isotopes have become a rather routine geochemical tool, its application/suitability as an environmental proxy for ancient sedimentary archives is still being explored ([Kasemann et al., 2014](#); [Pokrovsky et al., 2011](#)). Reconstruction of the $\delta^{26}\text{Mg}$ values of past seawater from carbonate deposits is highly challenging, as Mg isotope fractionation between the precipitated carbonate and ambient solution depends on multiple factors, e.g., temperature, precipitation rate and/

or alkalinity, as well as burial depth ([Blättler et al., 2015](#); [Mavromatis et al., 2013](#)). For these reasons, comparison of absolute values should be regarded with caution. However, trends and relative variations can be reasonably assessed. [Pokrovsky et al. \(2011\)](#) hypothesized that Mg isotope composition of Late Neoproterozoic sedimentary rocks or limestones/dolostones was mainly controlled by the weathering conditions and regime, i.e. carbonate vs. silicate weathering. The herein modelled $\delta^{26}\text{Mg}_{\text{carb}}$ values show a similar trend as the observed values at the Pc-C boundary (Figs. 5 and 6). For the Mg box model, the isotope composition of riverine input is crucial to the seawater $\delta^{26}\text{Mg}$ mass balance, revealing the important effect of continental silicate weathering on the observed $\delta^{26}\text{Mg}$ trend. Moreover, it excludes weathered carbonates (limestones and dolostones) as a major contributing factor to riverine run-off.

Our isotope modelling suggests that the ocean budget for Mg was close to steady state before and after the Pc-C boundary. During the transition, the Mg ocean budget was controlled by a simultaneous but incongruent increase of F_R and F_C , and consequently increasing hydrothermal activity (Fig. 5). As shown above (Section 4.2), this environmental scenario satisfies both Sr and Mg isotope trends in seawater, providing a feasible and coherent scenario for the observed isotope excursion. The conformity of both isotope systems (Mg and Sr) further justifies the use of Mg isotopes as a valid environmental proxy. However, due to the lack of comparison to other locations, the observed Mg isotope trend may have been driven by regional factors and may not be applicable to a global scale. Nonetheless, our study highlights the potential of Mg isotope investigations at the Pc-C boundary, and at similar critical episodes in Earth’s environmental history. As for most environmental proxies and especially for their applicability in ancient rocks, Mg isotopes should be applied within multi-proxy approaches.

5.3. The impact of silicate weathering on isotopic records

A global increase in continental weathering, as highlighted by a range of studies ([Shields, 2007](#); [Williams et al., 2019](#); [Zhang et al., 2014](#)), over the Pc-C transition affected individual $\delta^{13}\text{C}$ records within the litho- and hydrosphere. In general, secular (long-term) changes in the $\delta^{13}\text{C}$ records of carbonate deposits reflect mostly mixing of the organic and inorganic carbon pool, closely linked to climate changes, i.e., glacial and interglacial times. However, tectonic uplift and burial can also significantly affect the global carbon flux and mass balance ([Shields and Mills, 2017](#)). Simply speaking, increased continental reworking and thus a (silicate-) dominated riverine run-off into the ocean, as well as an increased supply of major nutrients enhance primary productivity in surface waters, effectively removing ^{12}C from the ocean causing high $\delta^{13}\text{C}$. Yet, the Pc-C boundary is marked by the negative basal Cambrian carbon excursion (BACE), also observed at the Koksui location (Fig. 2; [Stammeier et al., 2019a](#)). Generally, such a negative excursion towards more lighter $\delta^{13}\text{C}$ values in seawater is attributed to the oxidation of organic carbon, and/or the reworking of shallow-water carbonates during a transgression cycle ([Hoefs, 2015](#); [Pokrovsky et al., 2011](#); [Zuo et al., 2018](#)). [Shields and Mills \(2017\)](#) have shown that carbon contribution from intense silicate weathering outweighs the positive feedback loop of organic carbon removal. Given the significant contribution of silicate weathering to the ocean’s Mg and Sr budgets, as suggested in our model, this could be a likely scenario for the Pc-C boundary. Such an increase of continental silicate weathering caused the simultaneous increase of $\delta^{26}\text{Mg}$ and $^{87}\text{Sr}/^{86}\text{Sr}$ and decrease of $\delta^{13}\text{C}$ as observed at the Pc-C boundary (Fig. 2).

6. Palaeoenvironmental implications: long-term versus short-term environmental changes

Enhanced erosion rates are expected in the aftermath of several Neoproterozoic glaciations, such as e.g., during the Sturtian and Marinoan ([Kasemann et al., 2014](#)), and as a consequence of Gondwana

assembly from 0.8–0.6 Ga (Meert and Van Der Voo, 1997). Weathering and associated riverine run-off were thus the likely cause for the steady increase in Sr isotopes during the late Neoproterozoic era (cf. Halverson et al., 2010) along with an increase in ocean alkalinity and transport of nutrients, e.g., phosphorus, to the oceans (Smith and Harper, 2013).

The sharp excursion in seawater $^{87}\text{Sr}/^{86}\text{Sr}$ together with high $\delta^{26}\text{Mg}$ at the Pc-C transition (Fig. 2), however, indicates a single, critical geodynamic event. As demonstrated in our model, a short yet extreme change in all parameters (F_C , F_R , R_R), can result in the observed isotope trends. In the case of the Sr ocean budget, a time-interval of only 3 Myr of increased (silicate) weathering and associated “mineral reactivity” during this process was sufficient to trigger Sr isotope excursions. This cannot be solely explained by secular trends in enhanced weathering rates during the Neoproterozoic, but required a distinct geodynamic event. The timing coincided with a range of global orogenies, e.g., the Pan-African orogeny (ca. 870–550 Ma, Kröner and Stern, 2005), and the Cadomian orogeny (750–540 Ma, Linnemann et al., 2014), associated with the assembly of Gondwana. Whilst current geotectonic plate reconstruction lacks the temporal resolution to pinpoint a single, unique collisional event, the negative excursion in e.g., the global Hf isotope data, indicates an unprecedented collision of continental landmass at the time of Gondwana assembly (Roberts, 2012). Such a collisional event and the associated crustal reworking, including uplift, exposure, weathering and erosion, would have caused an increase of riverine input to the ocean, resulting in high, short-term $^{87}\text{Sr}/^{86}\text{Sr}$ and $\delta^{26}\text{Mg}$ values in the ocean.

7. Conclusions

Shallow-marine sedimentary deposits from the lowermost Cambrian succession close to the Pc-C boundary recorded coupled $^{87}\text{Sr}/^{86}\text{Sr}$ and $\delta^{26}\text{Mg}$ values with a distinct, positive isotope excursion. Isotope modelling demonstrated that the Pc-C transition was dominated by elevated weathering rates and carbonate formation. The positive excursions in seawater $^{87}\text{Sr}/^{86}\text{Sr}$ and $\delta^{26}\text{Mg}$ were caused by a short-term (ca. 3 Myr) increase in weathering rates and associated transport of weathered riverine material to the ocean. This resulted in distinctly high seawater $^{87}\text{Sr}/^{86}\text{Sr}$ and $\delta^{26}\text{Mg}$, which was rapidly counterbalanced by enhanced

hydrothermal activity. Modelling of seawater $^{87}\text{Sr}/^{86}\text{Sr}$ further suggests a shift from less radiogenic towards more radiogenic weathered material in the lead-up to the Pc-C transition. Together with elevated weathering rates, this agrees with progressing continental reworking and denudation in the aftermath of several global-scale glaciations and continental re-organization.

The modelled isotope data from the current study does only offer a first order, qualitative approximation, and in the case of Mg isotopes, might only reflect a local mechanism. However, the $^{87}\text{Sr}/^{86}\text{Sr}$ seawater evolution together with the model results for both Mg and Sr do support a severe, global-scale geodynamic event. The observed isotope excursions marking the Pc-C boundary at 541 Ma appear unique, both in their magnitude and relatively short duration. With this, they mirror the rapid biotic changes that occurred during the terminal Ediacaran and earliest Cambrian. It thus seems plausible that a geodynamic event, in this case continental collision along with reworking of evolved continental crust and an associated release of nutrients, led to a turnover in marine biota during the Pc-C transition.

Declaration of competing interest

The authors declare no conflict of interest.

Acknowledgements

Fieldwork was guided by G. Ergaliev and S. Zhemzhushnikov (Kazakh Academy of Science, Almaty). A special thanks to G. Franz and the members of DFG-FG 736 for the successful collaboration and support. J. Evers and P. Timm are thanked for SEM analyses. S. Perchthold is kindly thanked for assistance in the lab. I. Kell-Duivestein is kindly thanked for proof reading. This work was financially supported by the research project DFG-FG 736 (HI 1553/1-2, Deutsche Forschungsgemeinschaft, Germany) and NAWI Graz, Central Lab for Water, Minerals and Rocks (NAWI Graz Geocenter, Austria). ON acknowledges support from the Australian Research Council (FT140101062). The authors are also grateful to Xinyang Chen and one anonymous reviewer for constructive comments.

Appendix A. Supplementary data

Supplementary data to this article can be found online at <https://doi.org/10.1016/j.palaeo.2019.109452>.

APPENDIX A

ELEMENTAL AND ISOTOPE INFORMATION

Element and isotope compositions were determined on $3\text{ mol l}^{-1}\text{ HNO}_3$ leachates (compare methodology section). Main elemental concentrations reflect dissolution of mainly calcite, dolomite and carbonate-fluorapatite (CFA) and only trace amounts of detrital silicate cargo, that could contribute to bulk Mg isotope composition (compare table A2). Total main elemental concentrations were analysed at the Graz University of Technology by ICP-OES using an Optima 8300 (PerkinElmer, Waltham, USA) with an analytical precision of $\pm 2\%$.

Table A1

Total main elemental concentrations of the acid soluble fraction ($3\text{ mol l}^{-1}\text{ HNO}_3$; all elemental data from Stammeier et al. 2018. The abundance of CO_2 within the carbonates and phosphates was estimated from difference. n.a. = not available; < dl = below detection limit.

Sample	Al_2O_3 (wt. %)	CaO (wt. %)	Fe_2O_3 (wt. %)	MgO (wt. %)	Na_2O (wt. %)	P_2O_5 (wt. %)	SiO_2 (wt. %)	SUM (wt. %)	CO_2 (wt. %)
KO 1	0.36	49.6	5.09	4.57	0.59	37.8	0.21	98.2	1.80
KO 2	0.34	46.9	0.26	0.89	0.37	40.4	0.11	89.3	10.7
KO 3.1	0.42	41.1	0.16	6.44	D.L.	37.9	0.30	86.4	0.42
KO 3.2	0.30	46.1	1.46	2.37	0.28	37.0	0.03	87.5	12.5
KO 04	0.07	30.0	0.21	19.1	0.06	1.50	0.07	51.0	49.0
KO 6	0.28	48.5	2.48	2.87	0.23	35.2	0.04	89.6	10.4
KO 9	0.07	37.7	0.09	2.68	0.20	29.2	0.08	90.2	9.80
KO 10.1*	n.a.	n.a.	n.a.	n.a.	n.a.	n.a.	n.a.	n.a.	n.a.
KO 10.2*	0.06	73.0	0.02	2.34	0.21	28.5	0.08	70.0	30.0

(continued on next page)

Table A1 (continued)

Sample	Al ₂ O ₃ (wt. %)	CaO (wt. %)	Fe ₂ O ₃ (wt. %)	MgO (wt. %)	Na ₂ O (wt. %)	P ₂ O ₅ (wt. %)	SiO ₂ (wt. %)	SUM (wt. %)	CO ₂ (wt. %)
KO 11	0.04	43.0	0.01	2.98	0.21	35.9	0.03	104	n.a.
KO 12	0.03	39.1	0.01	5.99	0.18	27.7	0.03	82.2	17.8
KO 13.1*	n.a.	n.a.	n.a.	n.a.	n.a.	n.a.	n.a.	n.a.	n.a.
KO 13.2*	0.04	42.6	0.02	5.25	0.27	29.7	0.09	73.0	27.0.

n.a. = not analysed; * sample KO10.1 and KO13.1 reflect results from weak acid leachates (0.05 mol l⁻¹

HNO₃), KO10.2 and KO13.2 reflect results from strong acid leachates (3 mol l⁻¹

HNO₃, compare methodology section).

Table A2

Lithologic description of hand specimens and respective qualitative XRD results determining major mineral phases. Note that the order of minerals does not reflect quantitative results. Magnesium contents of the acid-soluble fraction (3 mol l⁻¹ HNO₃) are as reported in Stammeier et al., 2019a. Mg isotopes ($\delta^{25}\text{Mg}$ and $\delta^{26}\text{Mg}$ in ‰ DSM3) are reported as the mean of replica measurements with the uncertainty, expressed as 2 SD, referring to the standard deviation of the mean. In case the uncertainty of replica measurements is lower than the repeatability precision, values marked with *, the repeatability precision of $\pm 0.04\text{‰}$ for $\delta^{25}\text{Mg}$ and $\pm 0.10\text{‰}$ for $\delta^{26}\text{Mg}$ (2 SD, n = 23) for CAM-1 is reported.

Sample	Lithologic description	Mineralogy	MgO [wt. %]	$\delta^{25}\text{Mg}$ (‰DSM3)	± 2SD	$\delta^{26}\text{Mg}$ (‰DSM3)	± 2SD
KO 1	phosphatic chert	quartz, CFA, calcite	4.57	-0.21*	0.04	-0.45*	0.10
KO 2	phosphatic chert	quartz, CFA, calcite	0.89	-0.04*	0.04	0.06	0.12
KO 3.1	phosphatic chert	quartz, CFA, dolomite, calcite	2.37	-0.37	0.05	-0.77*	0.10
KO 3.2	phosphatic chert	n.a.	n.a.	0.25	0.04	0.48*	0.10
KO 04	cherty dolostone	quartz, CFA, dolomite	19.1	-0.34	0.09	-0.66	0.17
KO 6	phosphatic chert	quartz, CFA, dolomite, calcite	2.87	-0.23	0.22	-0.49	0.28
KO 9	phosphatic platy chert	quartz, CFA, dolomite, calcite	2.68	-1.16*	0.04	-2.12*	0.10
KO 10.1*	contact dolostone/phosphorite	quartz, CFA, dolomite, calcite	2.34	-0.59	0.05	-1.15*	0.10
KO 10.2*	phosphorite	n.a.	n.a.	-0.65*	0.04	-1.24*	0.10
KO 11	phosphorite	quartz, CFA, dolomite, calcite,	2.98	-1.01*	0.04	-1.91*	0.10
KO 12	dolomitic phosphorite	quartz, CFA, dolomite, calcite,	5.99	-0.66*	0.04	-1.42*	0.10
KO 13.1*	phosphatic flat pebble conglomerate	quartz, CFA, dolomite, calcite	5.25	-0.90*	0.04	-1.85*	0.10
KO 13.2*	phosphatic flat pebble conglomerate	n.a.	n.a.	-0.90	0.06	-1.69*	0.10

n.a. = not analysed; * sample KO10.1 and KO13.1 reflect results from weak acid leachates (0.05 mol l⁻¹

HNO₃), KO10.2 and KO13.2 reflect results from strong acid leachates (3 mol l⁻¹

HNO₃, compare methodology section).

PETROGRAPHY

The investigated phosphatic rock samples predominantly consist of different phos-grains of various grain size, with a calcite, dolomite or siliceous matrix. Phos-grains are often preserved as clasts (Fig. A1, Inset A and B), peloids or coated grains, such as oncoids and ooids. Scanning electron microscopy (SEM) images of phos-ooids and phos-peloids reveal the preservation of CFA nano-crystals, either as radially arranged prismatic CFA nanocrystals within the laminae of ooids (Fig. A1, Inset C) or as aggregated CFA nanocrystals within phos-peloids (Fig. A1, Inset D). Silica or dolomite cements the intergranular space. Rock fabrics thus consist of siliceous mudstone to grainstone phosphorite, the latter ranging from well-sorted phos-grainstones (Fig. A1, Inset B) to poorly sorted flat-pebble phos-rudstones (Fig. A1, Inset A). These rock fabrics indicate deposition in a shallow water environment, with pronounced phosphogenesis and subsequent reworking and deposition within a moderately to high energy setting.

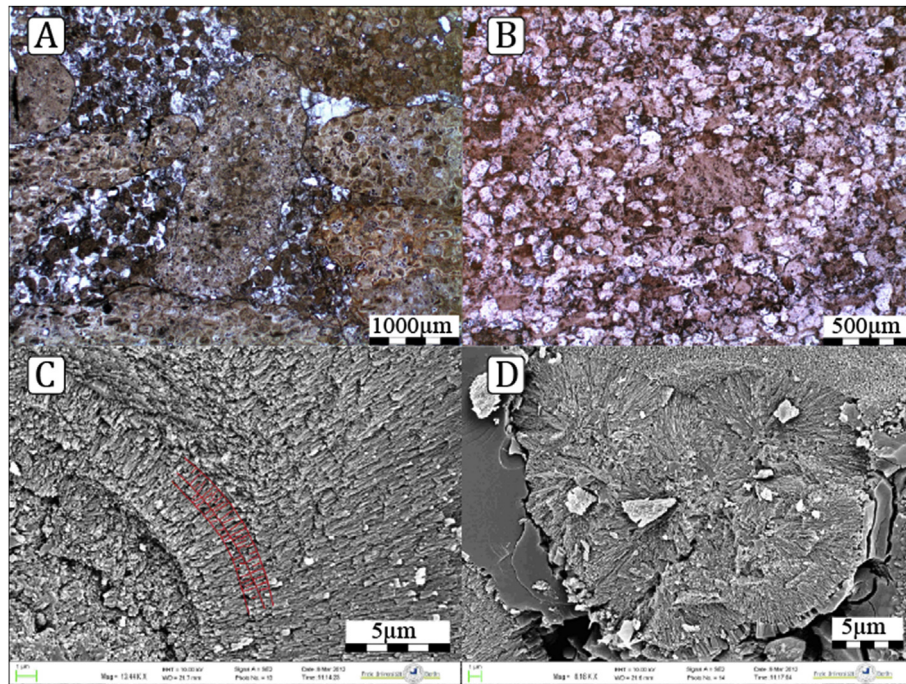


Fig. A1. Inset A: Poorly sorted flat-pebble phos-rudstone (KO 13) with a sparry dolomite matrix. Inset B: Well sorted phos-grainstone, with phos-clasts and few coated phos-grains within a sparry calcite cement (KO10, stained with Alizarin Red S). Inset C: Detailed SEM image of a phos-oid showing the well preserved prismatic CFA nanocrystals radially arranged within the laminae (KO13). Inset D: SEM image of a phos-peloid highlighting the radially-aggregated CFA nanocrystals (KO13).

References

- Aciego, S.M., Bourdon, B., Lupker, M., Rickli, J., 2009. A new procedure for separating and measuring radiogenic isotopes (U, Th, Pa, Ra, Sr, Nd, Hf) in ice cores. *Chem. Geol.* 266, 203–213. <https://doi.org/10.1016/j.chemgeo.2009.06.003>.
- Berner, R.A., Lasaga, A.C., Garrels, R.M., 1983. The carbonate-silicate geochemical cycle and its effect on atmospheric carbon dioxide over the past 100 million years. *Am. J. Sci.* 283, 641–683. <https://doi.org/10.2475/ajs.283.7.641>.
- Blättler, C.L., Miller, N.R., Higgins, J.A., 2015. Mg and Ca isotope signatures of authigenic dolomite in siliceous deep-sea sediments. *Earth Planet. Sci. Lett.* 419, 32–42. <https://doi.org/10.1016/j.epsl.2015.03.006>.
- Brasier, M.D., Shields, G.A., Kuleshov, V.N., Zhegallo, E.A., 1996. Integrated chemo- and biostratigraphic calibration of early animal evolution: Neoproterozoic–early Cambrian of southwest Mongolia. *Geol. Mag.* 133, 445–485. <https://doi.org/10.1017/S0016756800007603>.
- Burns, S.J., Haudenschild, U., Matter, A., 1994. The strontium isotopic composition of carbonates from the late Precambrian (560–540Ma). Huqf Group of Oman. *Chem. Geol.* 111, 269–282. [https://doi.org/10.1016/0009-2541\(94\)90094-9](https://doi.org/10.1016/0009-2541(94)90094-9).
- Caves Rugenstein, J.K., Ibarra, D.E., von Blanckenburg, F., 2019. Neogene cooling driven by land surface reactivity rather than increased weathering fluxes. *Nature* 571, 99–102. <https://doi.org/10.1038/s41586-019-1332-y>.
- Darroch, S.A.F., Smith, E.F., Laflamme, M., Erwin, D.H., 2018. Ediacaran extinction and cambrian explosion. *Trends Ecol. Evol.* 33, 653–663. <https://doi.org/10.1016/j.tree.2018.06.003>.
- de Villiers, S., Dickson, J.A.D., Ellam, R.M., 2005. The composition of the continental river weathering flux deduced from seawater Mg isotopes. *Chem. Geol.* 216, 133–142. <https://doi.org/10.1016/j.chemgeo.2004.11.010>.
- Derry, L.A., Brasier, M.D., Corfield, R.M., Rozanov, A.Y., Zhuravlev, A.Y.Y., 1994. Sr and C isotopes in Lower Cambrian carbonates from the Siberian craton: a paleoenvironmental record during the “Cambrian explosion.”. *Earth Planet. Sci. Lett.* 128, 671–681. [https://doi.org/10.1016/0012-821X\(94\)90178-3](https://doi.org/10.1016/0012-821X(94)90178-3).
- Eganov, E.A., Sovetov, K.Y., Yanoshin, A.L., 1986. Proterozoic and Cambrian phosphorite deposits: Karatau, southern Kazakhstan, USSR. In: Cook, P.J., Shergold, J.H. (Eds.), *Phosphate Deposits of the World*. Cambridge University Press, Cambridge, pp. 175–189.
- Fantle, M.S., Higgins, J.A., 2014. The effects of diagenesis and dolomitization on Ca and Mg isotopes in marine platform carbonates: implications for the geochemical cycles of Ca and Mg. *Geochim. Cosmochim. Acta* 142, 458–481. <https://doi.org/10.1016/j.gca.2014.07.025>.
- Farkaš, J., Chakrabarti, R., Jacobsen, S.B., Kump, L.R., Melezhik, V.A., 2013. Ca and Mg isotopes in sedimentary carbonates. In: Melezhik, V.A. (Ed.), *Reading the Archive of Earth's Oxygenation*. Springer-Verlag Berlin, Heidelberg, pp. 1468–1482. https://doi.org/10.1007/978-3-642-29670-3_10.
- Fox, D., 2016. What sparked the Cambrian explosion? *Nature* 530, 268–270. <https://doi.org/10.1038/530268a>.
- Geske, A., Goldstein, R.H., Mavromatis, V., Richter, D.K., Buhl, D., Kluge, T., John, C.M., Immenhauser, A., 2015a. The magnesium isotope ($\delta^{26}\text{Mg}$) signature of dolomites. *Geochim. Cosmochim. Acta* 149, 131–151. <https://doi.org/10.1016/j.gca.2014.11.003>.
- Geske, A., Lokier, S., Dietzel, M., Richter, D.K., Buhl, D., Immenhauser, A., 2015b. Magnesium isotope composition of sabkha porewater and related (Sub-)Recent stoichiometric dolomites, Abu Dhabi (UAE). *Chem. Geol.* 393–394, 112–124. <https://doi.org/10.1016/j.chemgeo.2014.11.020>.
- Halverson, G.P., Hurtgen, M.T., Porter, S.M., Collins, A.S., 2009. Neoproterozoic-cambrian biogeochemical evolution. In: Gaucher, C., Sial, A.N., Frimme, H.E., Halverson, G.P. (Eds.), *Neoproterozoic-Cambrian Tectonics, Global Change and Evolution: A Focus on South Western Gondwana*. Developments in Precambrian Geology, pp. 351–365. [https://doi.org/10.1016/S0166-2635\(09\)01625-01629](https://doi.org/10.1016/S0166-2635(09)01625-01629).
- Halverson, G.P., Wade, B.P., Hurtgen, M.T., Barovich, K.M., 2010. Neoproterozoic chemostratigraphy. *Precambrian Res.* 182, 337–350. <https://doi.org/10.1016/j.precamres.2010.04.007>.
- Heubeck, C., Ergaliev, G., Evseev, S., 2013. Large-scale seismogenic deformation of a carbonate platform straddling the precambrian-cambrian boundary, Karatau range, Kazakhstan. *J. Sediment. Res.* 83, 1004–1024. <https://doi.org/10.2110/jsr.2013.76>.
- Higgins, J.A., Schrag, D.P., 2010. Constraining magnesium cycling in marine sediments using magnesium isotopes. *Geochim. Cosmochim. Acta* 74, 5039–5053. <https://doi.org/10.1016/j.gca.2010.05.019>.
- Hodell, D.A., Mueller, P.A., McKenzie, J.A., Mead, G.A., 1989. Strontium isotope stratigraphy and geochemistry of the late Neogene ocean. *Earth Planet. Sci. Lett.* 92, 165–178. [https://doi.org/10.1016/0012-821X\(89\)90044-7](https://doi.org/10.1016/0012-821X(89)90044-7).
- Hoefs, J., 2015. *Stable isotope geochemistry*. Springer international publishing, cham. <https://doi.org/10.1007/978-3-319-19716-6>.
- Jackson, P., Attalla, M.I., 2010. N-Nitrosopiperazines form at high pH in post-combustion capture solutions containing piperazine: a low-energy collisional behaviour study. *Rapid Commun. Mass Spectrom.* 24, 3567–3577. <https://doi.org/10.1002/rcm>.
- Kasemann, S.A., Pogge von Strandmann, P.A.E., Prave, A.R., Fallick, A.E., Elliott, T., Hoffmann, K.H., 2014. Continental weathering following a Cryogenian glaciation: evidence from calcium and magnesium isotopes. *Earth Planet. Sci. Lett.* 396, 66–77. <https://doi.org/10.1016/j.epsl.2014.03.048>.
- Kröner, A., Stern, R.J., 2005. AFRICA | pan-african orogeny. In: *Encyclopedia of Geology*. Elsevier, pp. 1–12. <https://doi.org/10.1016/B0-12-369396-9/00431-7>.
- Laflamme, M., Darroch, S.A.F., Tweedt, S.M., Peterson, K.J., Erwin, D.H., 2013. The end of the Ediacara biota: extinction, biotic replacement, or Cheshire Cat? *Gondwana Res.* 23, 558–573. <https://doi.org/10.1016/j.jgr.2012.11.004>.
- Li, D., Ling, H.-F., Shields-Zhou, G.A., Chen, X., Cremonese, L., Och, L., Thirlwall, M., Manning, C.J., 2013. Carbon and strontium isotope evolution of seawater across the ediacaran–cambrian transition: evidence from the xiaotian section, NE yunnan, South China. *Precambrian Res.* 225, 128–147. <https://doi.org/10.1016/j.precamres.2012.01.002>.
- Li, W., Beard, B.L., Li, C., Xu, H., Johnson, C.M., 2015. Experimental calibration of Mg isotope fractionation between dolomite and aqueous solution and its geological

- implications. *Geochem. Cosmochim. Acta* 157, 164–181. <https://doi.org/10.1016/j.gca.2015.02.024>.
- Linnemann, U., Gerdes, A., Hofmann, M.H., Marko, L., 2014. The cadomian orogen: neoproterozoic to early cambrian crustal growth and orogenic zoning along the periphery of the west african craton—constraints from U–Pb zircon ages and Hf isotopes (schwarzburg antiform, Germany). *Precambrian Res.* 244, 236–278. <https://doi.org/10.1016/j.precamres.2013.08.007>.
- Mavromatis, V., Gautier, Q., Bosc, O., Schott, J., 2013. Kinetics of Mg partition and Mg stable isotope fractionation during its incorporation in calcite. *Geochem. Cosmochim. Acta* 114, 188–203. <https://doi.org/10.1016/j.gca.2013.03.024>.
- Mavromatis, V., Meister, P., Oelkers, E.H., 2014. Using stable Mg isotopes to distinguish dolomite formation mechanisms: a case study from the Peru Margin. *Chem. Geol.* 385, 84–91. <https://doi.org/10.1016/j.chemgeo.2014.07.019>.
- Meert, J.G., Van Der Voo, R., 1997. The assembly of Gondwana 800–550 Ma. *J. Geodyn.* 23, 223–235. [https://doi.org/10.1016/S0264-3707\(96\)00046-4](https://doi.org/10.1016/S0264-3707(96)00046-4).
- Nicholas, C.J., 1996. The Sr isotopic evolution of the oceans during the “Cambrian Explosion.”. *J. Geol. Soc. London* 153, 243–254. <https://doi.org/10.1144/gsjgs.153.2.0243>.
- Palmer, M.R., Edmond, J.M., 1989. The strontium isotope budget of the modern ocean. *Earth Planet. Sci. Lett.* 92, 11–26. [https://doi.org/10.1016/0012-821X\(89\)90017-4](https://doi.org/10.1016/0012-821X(89)90017-4).
- Pogge von Strandmann, P.A.E., 2008. Precise magnesium isotope measurements in core top planktic and benthic foraminifera. *Geochem. Geophys. Geosyst.* 9, 1–13. <https://doi.org/10.1029/2008GC002209>.
- Pogge von Strandmann, P.A.E., Forshaw, J., Schmidt, D.N., 2014. Modern and Cenozoic records of seawater magnesium from foraminiferal Mg isotopes. *Biogeosciences* 11, 5155–5168. <https://doi.org/10.5194/bg-11-5155-2014>.
- Pokrovsky, B.G., Mavromatis, V., Pokrovsky, O.S., 2011. Co-variation of Mg and C isotopes in late Precambrian carbonates of the Siberian Platform: a new tool for tracing the change in weathering regime? *Chem. Geol.* 290, 67–74. <https://doi.org/10.1016/j.chemgeo.2011.08.015>.
- Richter, F.M., Rowley, D.B., DePaolo, D.J., 1992. Sr isotope evolution of seawater: the role of tectonics. *Earth Planet. Sci. Lett.* 109, 11–23. [https://doi.org/10.1016/0012-821X\(92\)90070-C](https://doi.org/10.1016/0012-821X(92)90070-C).
- Roberts, N.M.W., 2012. Increased loss of continental crust during supercontinent amalgamation. *Gondwana Res.* 21, 994–1000. <https://doi.org/10.1016/j.gr.2011.08.001>.
- Sawaki, Y., Ohno, T., Fukushi, Y., Komiya, T., Ishikawa, T., Hirata, T., Maruyama, S., 2008. Sr isotope excursion across the Precambrian–Cambrian boundary in the Three Gorges area, South China. *Gondwana Res.* 14, 134–147. <https://doi.org/10.1016/j.gr.2007.11.002>.
- Shields, G.A., 2007. A normalised seawater strontium isotope curve: possible implications for Neoproterozoic–Cambrian weathering rates and the further oxygenation of the Earth. *eEarth* 2, 35–42. <https://doi.org/10.5194/ee-2-35-2007>.
- Shields, G.A., Mills, B.J.W., 2017. Tectonic controls on the long-term carbon isotope mass balance. *Proc. Natl. Acad. Sci.* 114, 4318–4323. <https://doi.org/10.1073/pnas.1614506114>.
- Smith, M.P., Harper, D.T., 2013. Causes of the cambrian explosion. *Science* 341, 1355–1356. <https://doi.org/10.1126/science.1239450>. (80-).
- Stammeier, J.A., Hippler, D., Nebel, O., Leis, A., Grengg, C., Mittermayr, F., Kasemann, S.A., Dietzel, M., 2019a. Radiogenic Sr and stable C and O isotopes across pre-cambrian-cambrian transition in marine carbonatic phosphorites of Malyi Karatau (Kazakhstan)—Implications for paleo-environmental change. *Geochem. Geophys. Geosyst.* 20, 3–23. <https://doi.org/10.1029/2018GC007767>.
- Stammeier, J.A., Nebel, O., Hippler, D., Dietzel, M., 2019b. MethodsX. Stable Magnesium and Radiogenic Strontium Isotopes in Carbonate Bearing Geologic Reference Materials (SARM 40, SARM 43, SRM 88A, SRM 88B) (Submitted).
- Tipper, E.T., Galy, A., Bickle, M.J., 2008. Calcium and magnesium isotope systematics in rivers draining the Himalaya–Tibetan–Plateau region: lithological or fractionation control? *Geochem. Cosmochim. Acta* 72, 1057–1075. <https://doi.org/10.1016/j.gca.2007.11.029>.
- Tipper, E.T., Galy, A., Bickle, M.J., 2006a. Riverine evidence for a fractionated reservoir of Ca and Mg on the continents: implications for the oceanic Ca cycle. *Earth Planet. Sci. Lett.* 247, 267–279. <https://doi.org/10.1016/j.epsl.2006.04.033>.
- Tipper, E.T., Galy, A., Gaillardet, J., Bickle, M.J., Elderfield, H., Carder, E.A., 2006b. The magnesium isotope budget of the modern ocean: constraints from riverine magnesium isotope ratios. *Earth Planet. Sci. Lett.* 250, 241–253. <https://doi.org/10.1016/j.epsl.2006.07.037>.
- Wilkinson, B.H., Algeo, T.J., 1989. Sedimentary carbonate record of calcium–magnesium cycling. *Am. J. Sci.* 289, 1158–1194. <https://doi.org/10.2475/ajs.289.10.1158>.
- Williams, J.J., Mills, B.J.W., Lenton, T.M., 2019. A tectonically driven Ediacaran oxygenation event. *Nat. Commun. Now.* 10 (2690). <https://doi.org/10.1038/s41467-019-10286-x>.
- Wilson, M.B., 1989. *Igneous petrogenesis*. Springer, Netherlands. <https://doi.org/10.1007/978-1-4020-6788-4>. Dordrecht.
- Wimpenny, J., Yin, Q.Z., Tollstrup, D., Xie, L.W., Sun, J., 2014. Using Mg isotope ratios to trace Cenozoic weathering changes: a case study from the Chinese Loess Plateau. *Chem. Geol.* 376, 31–43. <https://doi.org/10.1016/j.chemgeo.2014.03.008>.
- Wombacher, F., Eisenhauer, A., Heuser, A., Weyer, S., 2009. Separation of Mg, Ca and Fe from geological reference materials for stable isotope ratio analyses by MC-ICP-MS and double-spike TIMS. *J. Anal. At. Spectrom.* 24, 627–636. <https://doi.org/10.1039/b820154d>.
- Zhang, X., Shu, D., Han, J., Zhang, Z., Liu, J., Fu, D., 2014. Triggers for the cambrian explosion: hypotheses and problems. *Gondwana Res.* 25, 896–909. <https://doi.org/10.1016/j.gr.2013.06.001>.
- Zuo, J., Peng, S., Qi, Y., Zhu, X., Bagnoli, G., Fang, H., 2018. Carbon-isotope excursions recorded in the cambrian system, South China: implications for mass extinctions and sea-level fluctuations. *J. Earth Sci.* 29, 479–491. <https://doi.org/10.1007/s12583-017-0963-x>.